Experiments in Fluids (2024) 65:152
https://doi.org/10.1007/s00348-024-03880-3

RESEARCH ARTICLE

Volumetric wake investigation of a free-flying quadcopter using Shake-The-Box Lagrangian particle tracking

C. Christian Wolf[1] · Daniel Schanz[1] · Clemens Schwarz[1] · Alexander Heintz[1] · Johannes Bosbach[1] · Tobias Strübing[1] · Andreas Schröder[1,2]

Received: 19 July 2024 / Revised: 30 August 2024 / Accepted: 1 September 2024 / Published online: 2 October 2024

Abstract

The Shake-The-Box technique was applied to experimentally quantify the time-resolved volumetric flow field around a free-flying quadcopter UAV with an overall span of about 0.5 m. State-of-the-art LED illumination and high-speed camera equipment was combined with modern Lagrangian tracer particle tracking and data assimilation techniques, facilitating a measurement volume larger than 1.5 m^3. The setup allowed for both hover and limited maneuvering of the quadcopter, while resolving even small details of the complex interactional aerodynamics. In hover out of ground effect, the four individual rotor wakes merged into a single jet within a few rotor radii below the rotor planes. Evaluating the mass and momentum fluxes over suitable control volumes yields accurate estimates for the quadcopter's total thrust, the asymmetric thrust distribution between front and back rotors, and the entrainment of external flow through turbulent mixing. Hover in ground effect decreases the power requirement and induces recirculating flow in the center of the four rotors. The outwash pattern is non-uniform with jets developing between the rotors and pointing in radially outward directions. Forward flight cases result in a skewed, rapidly merging wake flanked by the roll-up of two "supervortices" similar to the wingtip vortices of fixed-wing vehicles.

List of symbols

A_r	Rotor area (four rotors), $A_r = 0.152\,m^2$
C_T	Thrust coefficient
dA	Area increment, m^2
D	Rotor diameter, $D = 0.22\,m$
F_z	Force in z-direction, N
g	Gravitational accel., $g = 9.81\,m/s^2$
h	Height above ground, m
m	Gross mass, kg
n	Rotational frequency, Hz
$\vec{n}$	Normal unit vector, area increment dA
P	Rotor pitch, $P = 0.11\,m$
Q	Q-criterion (vortex identification), $1/s^2$
R	Rotor radius, $R = 0.11\,m$
T	Rotor thrust, N
$\vec{u}$	Velocity vector, m/s
u, v, w	Veloc. compon. x, y, z-direction, m/s
V_h	Hover-induced velocity, m/s
v_r	Radial vel. comp. in x, y-plane, m/s
x, y, z	Cartesian coordinates, m
Δ	Difference between two values
ρ	Air density, kg/m^3
CFD	Computational fluid dynamics
CV	Control volume
DLR	German Aerospace Center
eVTOL	Electric vertical take-off and landing aircraft
GNSS	Global navigation satellite system
HFSB	Helium-filled soap bubbles
IGE	In ground effect

✉ C. Christian Wolf
Christian.Wolf@DLR.de

Daniel Schanz
Daniel.Schanz@DLR.de

Clemens Schwarz
Clemens.Schwarz@DLR.de

Alexander Heintz
Alexander.Heintz@DLR.de

Johannes Bosbach
Johannes.Bosbach@DLR.de

Tobias Strübing
Tobias.Struebing@DLR.de

Andreas Schröder
Andreas.Schroeder@DLR.de

[1] Institute of Aerodynamics and Flow Technology, German Aerospace Center (DLR), Bunsenstr. 10, Göttingen 37085, Germany

[2] Chair of Image Based Measurement Techniques, Brandenburg University of Technology, Platz der Deutschen Einheit 1, Cottbus 03013, Germany

LED	Light-emitting diode
OGE	Out of ground effect
STB	Shake-The-Box
Std	Standard deviation
UAV	Unmanned aerial vehicle

1 Introduction

The recent interest in eVTOL configurations encourages aerodynamic investigations of vehicles with distributed, speed-controlled rotor systems rather than swashplate-actuated main rotor/tail rotor designs as used on conventional helicopters. Operating multiple rotors in close proximity results in interactional effects, including deviations from the behavior and performance of single isolated rotors, e.g., see Shukla and Komerath (2018). For smaller unmanned aerial vehicles (UAVs), the quadcopter with a simple square layout (two front rotors, two back rotors) is arguably the most common design choice due to its simplicity. Larger manned vehicles tend to use a larger number of lift rotors, providing additional redundancy and limiting the diameter and, thus, the inertia of each individual variable-speed rotor.

Due to its relevance for smaller configurations, the quadcopter layout has been studied by a multitude of numerical investigations, e.g., see Lim and Thai (2023); Kostek et al. (2024); Yoon et al. (2017); Ventura Diaz and Yoon (2018); Shirazi (2022). The numerical methods in the cited references range from mid-fidelity approaches, for example lifting line or panel methods coupled to free wake models, up to state-of-the-art computational fluid dynamics (CFD). In addition to a variation of the quadrotor's geometric and rotational parameters, the influences of forward flight and ground effect have been identified as important key factors for interactional aerodynamics.

Yonezawa et al. (2021) and Tanabe et al. (2021) used JAXA's "rFlow3D" CFD solver to study a mid-sized quadcopter ($m = 7$ kg) with two-bladed rotors ($D = 0.38$ m) and a generic fuselage hovering both in and outside of ground effect (IGE/OGE), which is highly relevant to the current test cases. Among other results, Yonezawa et al. (2021) predict that a smaller rotor-to-rotor separation does not affect the OGE power requirement but reduces the IGE power requirement. An analysis of the volumetric flow field implies that this is due to the occurrence of a stronger recirculation and, thus, a stronger upwash in the center of the rotors. Moreover, IGE hover yields an azimuth-dependent outwash pattern with strong jets developing between the individual rotors. Cross-comparisons with experimental results are highly desirable due to the complexity of the flow and due to numerical uncertainties, as also pointed out by the quadcopter studies of Kostek et al. (2024) and Shirazi (2022).

Particle image velocimetry (PIV) is a standard measurement technique and can be applied to experimentally quantify the flowfield resulting from rotor–rotor interactions. This was, for example, demonstrated in subscale tests of stacked coaxial rotors by De Gregorio et al. (2023), side-by-side rotors by Shukla and Komerath (2018) and Nargi et al. (2021), or quadcopter configurations by Otsuka et al. (2017) and Throneberry et al. (2022). However, the velocity data are restricted to two-dimensional measurement planes, which can be inadequate for complex and azimuthally varying flow geometries.

A possible solution is the application of the volumetric Shake-The-Box (STB) particle tracking method, see Schröder and Schanz (2023). In comparison with other volumetric methods such as tomographic PIV, STB can be applied at higher particle image densities and yields a higher local resolution due to the tracking of individual particles at approximately 0.1 px accuracy. Especially when applied to large-scale measurements, particle tracking is much more efficient, as the voxel-spaces and their correlation applied by tomographic PIV require an enormous amount of memory and computational resources.

For STB, the density of individually traceable seeding particles for a given camera resolution can be high, thanks to a time-marching particle trajectory prediction/correction step using time-resolved image data. Furthermore, the Lagrangian velocity and acceleration data of the particles can be assimilated to volumetric result data using additional physical constraints, e.g., conservation of mass assuming incompressible flow, to further increase the spatial resolution.

So far, very few applications of STB to rotor flows have been reported. In our previous work, see Wolf et al. (2019), the measurement technique was used to prove the existence of secondary vortex structures stretching between the primary blade tip vortices in the wake of a model helicopter. Only a part of the entire rotor azimuth was covered by the measurement volume with a size slightly smaller than 0.1 m^3. The results were a starting point for successful comparisons to high-fidelity CFD simulations, e.g., using the Helios framework as demonstrated by Bodling and Potsdam (2022); Bodling et al. (2024). Schröder et al. (2023) applied STB to investigate the flow field in the near wake of a one-bladed model rotor in hover conditions, concentrating on the instabilities of a twin-helix tip vortex system generated by the addition of a fin to the rotor blade tip. Most relevant for the current publication, Dekker et al. (2022) studied regions of separated and recirculating (fountaining) flow in the wake of two side-by-side rotors ($D = 0.076$ m) in ground effect. Different flow regimes were identified, based on the geometric parameters of ground clearance and rotor separation. The rotor system was mounted in a test enclosure

with a volume of 12 m^3, and the STB measurement volume was approx. 0.02 m^3. Furthermore, Viola et al. (2022) set up an underwater STB system to study the tip vortices of a three-bladed tidal turbine ($D = 1.2$ m). The instantaneous measurement volume was only 0.012 m^3, but it was traversed along the turbine's wake to increase the overall measurement volume.

The current work combines state-of-the-art hardware, comprising advanced high-speed cameras and LED volume illumination, to improved data acquisition and evaluation strategies (two-stage scanning), resulting in a large measurement volume (> 1.5 m^3) with a sufficient spatial resolution (approximately 5 mm). The setup enables, to our knowledge for the first time, a time-resolved acquisition of the entire volumetric flow field around a free-flying quadcopter drone with a total span of about 0.5 m.

2 Experimental setup

2.1 Quadcopter

The current study used the radio-controlled consumer drone "DJI Mavic 2 Pro," see Fig. 1 and DJI (2024), with four two-bladed rotors (diameter $D = 0.22$ m, pitch $P = 0.11$ m) arranged in an "X-layout." The front rotors are horizontally separated by 1.35 D and counterrotate in "bearhug" mode, whereas the back rotors operate in "breaststroke" mode with a separation of 1.17 D. The entire configuration can be termed "square bearhug." The horizontal clearance between front and back rotor tips is zero, but the front rotors are vertically offset by 0.18 D. The rotor planes feature an inward tilt (anhedral), with included angles between about 6 deg and

Fig. 1 Quadcopter DJI Mavic 2 Pro, the nose points downward, note the payload ballast plate (here: 220 g) on top of the fuselage

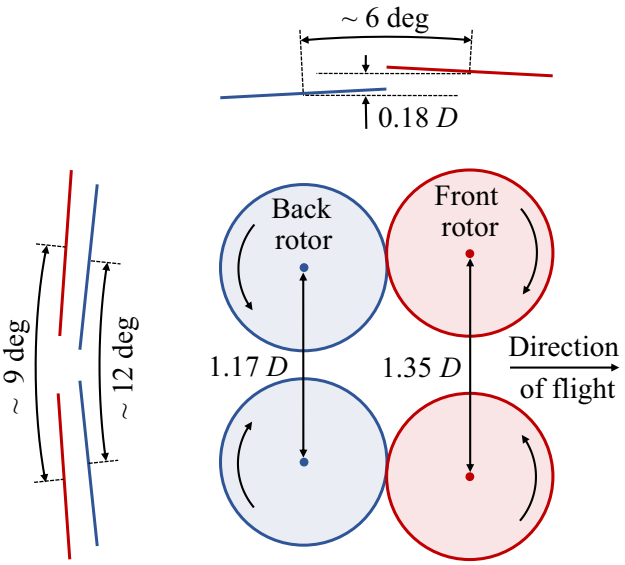

Fig. 2 Layout of the rotor planes, showing top-down and side views

12 deg between pairs of rotor axes, see the sketch in Fig. 2 for further reference.

The inward tilt angles of the rotors can have a positive effect on the static stability at the cost of a reduced gust rejection capability, see Whidborne et al. (2022) for details, but the reasoning behind the manufacturer's design choices are not known to the authors.

The fuselage and the rotor struts were covered with a matte black foil to reduce reflections of the measurement illumination system. The standard remote flight controller of the drone and its control laws were used during the tests, with the GNSS positioning and the automatic collision avoidance switched off for operation in an indoor test enclosure and close to the ground. Both hover test cases in different heights and forward flight cases up to a speed of approximately 3 m/s were commanded by manual piloting.

Using the drone's payload capacity, the standard gross mass of 915 g could be increased by attaching steel plates (220 g or 440 g) with velcro tape to the top surface of the fuselage and close to the center of mass. This yields a variation of the hover-induced velocity between $V_h = 4.9$ m/s and $V_h = 6.1$ m/s. V_h is calculated via

$$V_h = \sqrt{\frac{T}{2\rho A_r}} \tag{1}$$

with the area of all four rotors, $A_r = 0.152\,m^2$. The total thrust is approximated with the known gross mass via $T \approx m\,g$, neglecting the fuselage download and interactional effects. Table 1 shows the average rotational frequencies of the front and back rotors in hover outside of ground effect (OGE) and for different gross masses. The

Table 1 Rotor system performance data for OGE hover

m	n (front)	n (back)	V_h	C_T
915 g	94 Hz	81 Hz	4.9 m/s	0.0134
1135 g	105 Hz	90 Hz	5.5 m/s	0.0134
1355 g	115 Hz	98 Hz	6.1 m/s	0.0134

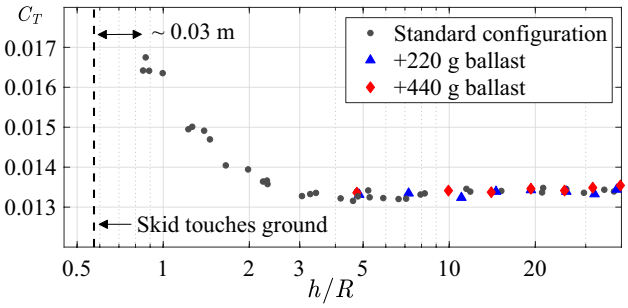

Fig. 3 Average rotor thrust coefficient as a function of the hover height, note the logarithmic abscissa

data were acquired after the flight tests via readout of the onboard flight controller, and additionally checked with a high-speed camera. It is noted that the speed of the front rotors is approximately 17% higher in comparison with the back rotors, resulting from a front-heavy mass distribution. Depending on the varying air density of the experiments, the thrust coefficient is $C_T = 0.0134 - 0.0136$ using

$$C_T = \frac{T}{\rho A_r (n\pi D)^2} \tag{2}$$

with the frequency n set to the average of all four rotors, and again using $T \approx m\,g$. A more detailed analysis of the total net thrust and the thrust split is given in Sect. 3.2 by means of a momentum analysis applied to the volumetric flow data. Increasing the payload yields a corresponding increase in the rotor speed at a constant C_T, indicating that even the highest payload does not cause rotor blade stall.

Figure 3 shows the thrust coefficient as a function of the normalized hover height, h/R, defined as the vertical distance between the ground surface and the geometric center between front and back rotor planes. Decreasing the hover height below three rotor radii ($h = 0.33$ m) results in an increasing rotor efficiency inside ground effect (IGE). Consequently, the decreasing rotor frequency at a constant gross mass yields an increasing C_T, with a maximum of about $C_T = 0.0170$ shortly before the quadcopter's skid touches the ground. It is noted that the data in Fig. 3 is similar to the results of previous quadcopter performance studies, for example see Sanchez-Cuevas et al. (2017), but the exact thrust curve depends on the parameters of the rotor system.

2.2 Shake-The-Box setup

The experiments were conducted in a test enclosure with a rectangular main chamber sized 6 m × 4 m × 2.8 m = 67.2 m^3, see Fig. 4. The side and back walls consisted of plywood panels painted black, and large polycarbonate glass panels were used as a front wall to enable optical access for the camera system. A tent-like black cloth cover was used as a ceiling to provide additional volume and to reduce the interference with the quadcopter's inflow, adding up to a total enclosure volume of about 84 m^3. With the estimated volume flow through the rotor planes, $A_r \cdot V_h = 0.745$ m^3/s (see Table 1, $V_h = 4.9$ m/s without additional ballast), it takes the quadcopter about 113 s to circulate the entire air volume. The enclosure is required due to the limited lifespan of the helium-filled soap bubbles (HFSB, diameter approx. 350 mm) serving as flow tracers, and due the limited output rate of the seeding system with about 1.5 million HFSB per second. Furthermore, the enclosure protects the delicate measurement equipment, particularly the cameras, from contact with the bubbles.

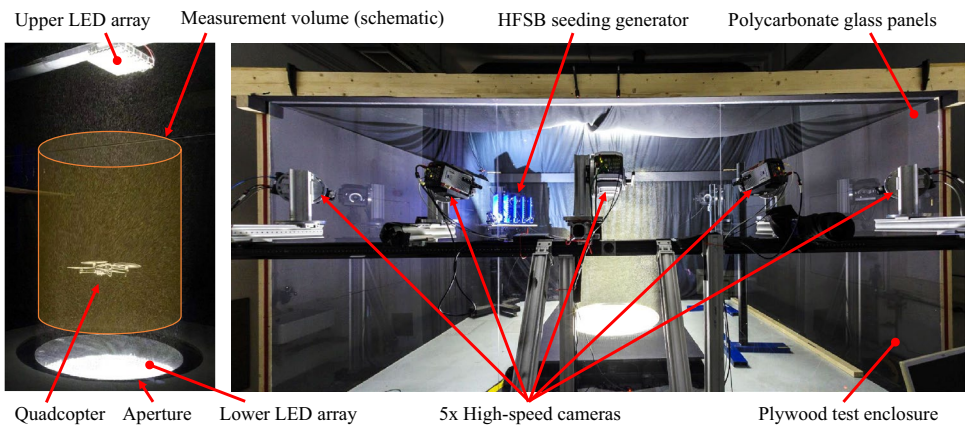

Fig. 4 Quadcopter hovering in the illuminated measurement volume seeded with flow tracers (left), overview of the test enclosure and camera system (right)

Illumination of the measurement volume was provided by DLR-designed pulsed LED arrays, producing white light pulses at a rate of 3 kHz, corresponding to approximately 30 pulses per rotor revolution. A large rectangular array (1.6 m × 1.6 m) with 1600 individual LEDs was installed under a floor plate with a circular aperture ($D = 1.25$ m), projecting a cylindrical light column with low angular divergence in upward direction. A second smaller array was mounted at the ceiling, pointing downward to illuminate the shadow region above the quadcopter, also see Fig. 4 (left). A system of five Vision Research Phantom high-speed cameras (4× type "v2640," 1× type "v1840") with a sensor size of 4 Mpx observed the flow tracers through the front glass, arranged on a circular arc with an enclosed angle of about 90 deg and with a distance of about 2.5 m to the center of the measurement volume, see Fig. 4 (right). The camera optics (Carl Zeiss 50 mm Planar and 60 mm Makro-Planar) were chosen so that the fields of view cover the entire width of the light column and a height of about 1.75 m above ground. The three-dimensional camera calibration was accomplished using images of a regular dot-pattern plate traversed trough the measurement volume. In a second stage, the calibration was refined using Volume Self-Calibration, see Wieneke (2008), and a calibration of the optical transfer function, see Schanz et al. (2013). Figure 5 shows a top-down sketch of the test setup, with the dimensions and positions of the main components in scale.

A high volumetric seeding density was achieved using the novel approach of "scanning two-stage illumination" introduced by Schanz et al. (2024), in which the front and back halves of the LED arrays were triggered with an offset of half a time step. The resulting sub-volumes were acquired individually thanks to a doubled camera frame rate (6 kHz instead of 3 kHz), increasing the maximum possible number of flow tracers in the combined volume for a given camera sensor size.

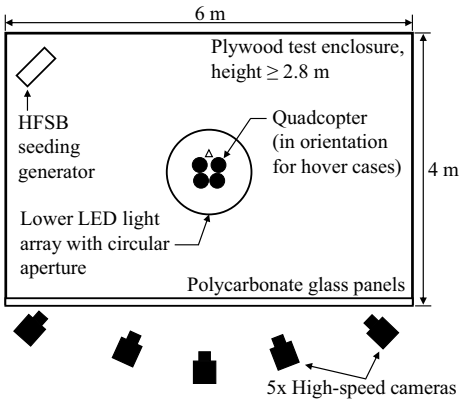

Fig. 5 Top-down sketch of the test setup, dimensions and positions are shown to scale

In each test case, 8400 samples were acquired for each of the scanning volumes, corresponding to a time interval of 2.8 s. More than 400000 HFSB tracers were tracked in every time step, for an image sensor size of 4 Mpx resulting in a density of about 0.1 particle images per pixel. The phase or azimuth angle of individual rotors during the Shake-The-Box measurements is unknown and arbitrary. Differing from the time-averaged rotor speeds in Table 1, the flight controller shows transient frequency changes due to station-keeping control inputs, and left–right differences due to manufacturing tolerances of the blades. For the given measurement interval and the large number of flow samples, it is assumed that the time-averaged flow fields are not biased by phase-locking issues.

The image evaluation via DLR's implementation of the Shake-The-Box principle, see Schanz et al. (2016), using the variable time-step approach, see Schanz et al. (2021), yields the time-resolved three-dimensional tracks of the identified flow tracers. Applying DLR's data assimilation method "FlowFit" by Gesemann et al. (2016) with incompressible Navier–Stokes constraints (here: conservation of mass, assuming incompressible flow) then provides a continuous representation of the flow's time-resolved velocity distributions.

2.3 Data analysis and post-processing

For the subsequent data analysis, the continuous FlowFit representation of the flowfield was restricted to a smaller rectangular subvolume, based on the position of the quadcopter in the overall measurement volume, and sampled on a Cartesian grid with a resolution of 5 mm (0.045 R) in all x, y, z-directions. For further data reduction, the temporal resolution was undersampled at 750 Hz (every fourth camera image of the flow tracers, or about eight samples per rotor revolution). Figure 6 shows an instantaneous sample of an IGE hover case with $m = 1135$ g at $h/R = 3$ above ground.

Isosurfaces of the Q-criterion (threshold value $3 \times 10^4/\mathrm{s}^2$) visualize small-scaled vortical structures developing in the wake below the quadcopter, before convecting along the ground surface in radially outward direction. Despite the lack of a dense tracer seeding in the rotor planes (details will be discussed in the next section), the FlowFit data assimilation still clearly reveals four toroidal vortical structures, driven by the blade tip vortices and marking the blade tip planes of the rotors. Even though the data are not suitable for an in-depth analysis of the tip vortex properties, it was used to determine the quadcopter's position in hover cases. Therefore, the instantaneous fields were averaged over short time intervals of 0.167 s (about 15 rotor revolutions) for a clear visualization of the tip planes, and the center of each rotor plane was selected manually. The coordinate origin was then set to the geometric center of the four rotor plane

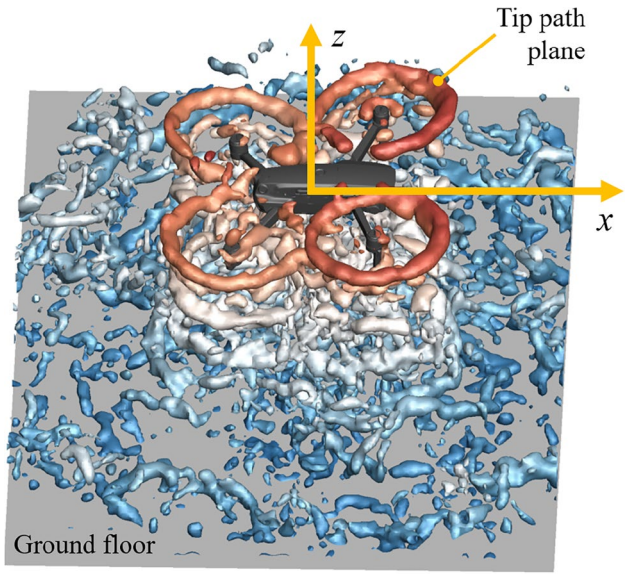

Fig. 6 Top right view, IGE hover at $h/R = 3$, instantaneous isosurfaces $Q = 3 \times 10^4/\mathrm{s}^2$. The red-to-blue coloring corresponds to a decreasing z-position from $z/R = 0.3$ to $r/R = -3.0$

centers, with the x-axis pointing horizontally in forward flight direction and the z-axis pointing vertically up, against the direction of gravity. This coordinate system is shown in Fig. 6, together with a 3D model of the quadcopter's fuselage (dark gray surfaces) for illustration purposes. During the overall test interval of 2.8 s, the center of the quadcopter usually drifted several centimeters in random directions. The LED illumination in the ground surface probably interfered with the quadcopter's internal downward vision system used for automatic position stabilization, yielding a notably larger drift compared to "light-off" conditions. Correcting this drift allows to calculate the flow statistics in a quadcopter-fixed coordinate system. The average horizontal drift velocity for all hover cases in this study is 0.034 m/s, with an instantaneous maximum of 0.105 m/s. In relation to the quadcopter's hover-induced velocity, $V_\mathrm{h} = 4.9\,\mathrm{m/s}$ after Table 1, no pronounced forward flight effects are expected, even though asymmetries in the flow field (discussed later) may be a result from the drift.

2.4 Seeding density and particle voids

Figure 7 shows a detail of a grayscale-inverted raw camera image, with only 850×500 px out of a total size of 1952×2048 px. The quadcopter is in forward flight left to right. Depending on the camera positions, the fuselage and the rotors will obstruct the view and interfere with the STB particle tracking.

Figure 8 shows HFSB particle tracks for a standard OGE hover case with $m = 915\,\mathrm{g}$, and for ten subsequent flow

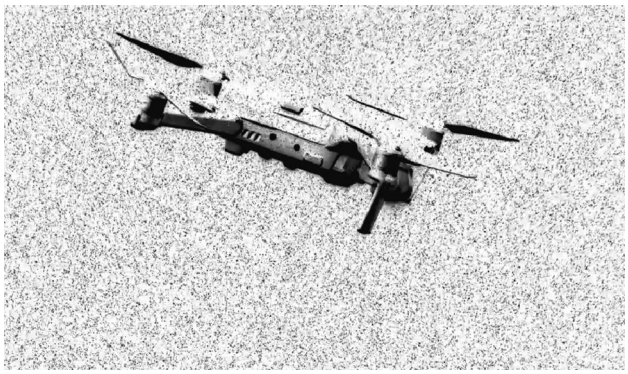

Fig. 7 Detail of a raw camera image with inverted grayscale

samples taken at 3 kHz. For simplicity, the figure only considers tracks up- and downstream of the left back rotor plane, which is visualized by a semi-transparent disk with corresponding motor nacelle and strut. The tracks of individual particles appear as dotted lines with predominantly vertical alignment, and the spacing increases from top to bottom due to the flow's acceleration.

The rotor plane itself and the area of the motor strut suffer from a very small density of identified particles, motivating a statistical analysis over the entire measurement interval

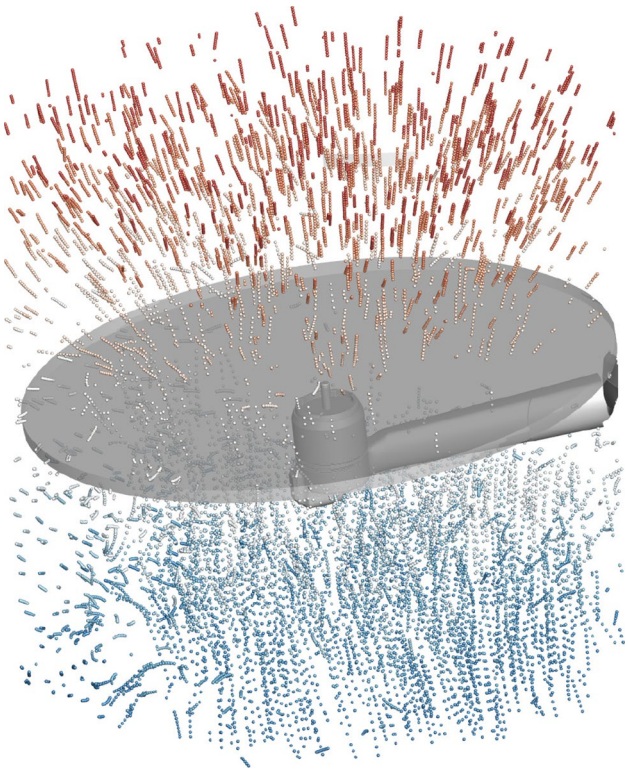

Fig. 8 Particle tracks close to the left back rotor, 10 time steps sampled at 3 kHz. The red-to-blue coloring corresponds to a decreasing z-position from $z/R = 0.8$ to $r/R = -1.2$

of 2.8 s. The result is the average particle count per grid point, referring to the final Cartesian sampling result with a spacing of $\Delta(x, y, z) = 5$ mm in the quadcopter's reference. Above the left back rotor plane at $z/R = 0.8$ (not shown), the seeding is homogeneous with a density of 0.039 particles per grid point. Due to the volumetric nature of the data, this corresponds to $\sqrt[3]{0.039} = 0.34$ particles per grid point in each (x, y, z)-direction. In large parts of the rotor plane at $z \approx 0$ (not shown), the average number of tracked tracer particles is close to zero due to the rotor blades obstructing the view of the cameras, yielding unreliable velocity results. A positioning of additional cameras on the opposite side of the measurement volume would have mitigated this effect, but was not feasible for this investigation.

Shortly below the rotor plane at $z/R = -0.4$ is a wedge-shaped area with low particle count, see the right half of the top-down view in Fig. 9a. This area results from the rotor's support beam obstructing the view of the cameras mounted left outside of the image. In addition, there is a circular arc of low particle count resulting from the voids in the blade tip vortices exerting strong centrifugal forces. Further below at $z/R = -0.8$, see Fig. 9b, the blade tip void is still visible, but the particle density has recovered elsewhere. The average of 0.037 particles per grid point approaches the inflow density above the rotor. This means that even though the rotors and the fuselage structure interrupt the optical particle tracking, the rotor blades do not eliminate the delicate HFSB tracer bubbles in large numbers, which would result in a reduced particle density below the rotor.

In its current version, the FlowFit data assimilation provides velocity data even in areas with insufficient particle densities, which can be seen as an extrapolation under the conservation of mass-constraint. The results in this paper will therefore include the 3D model of the quadcopter for illustration and orientation purposes, and quantitative analyses (for example, a later thrust calculation via the momentum fluxes) will exclude the low-seeding areas.

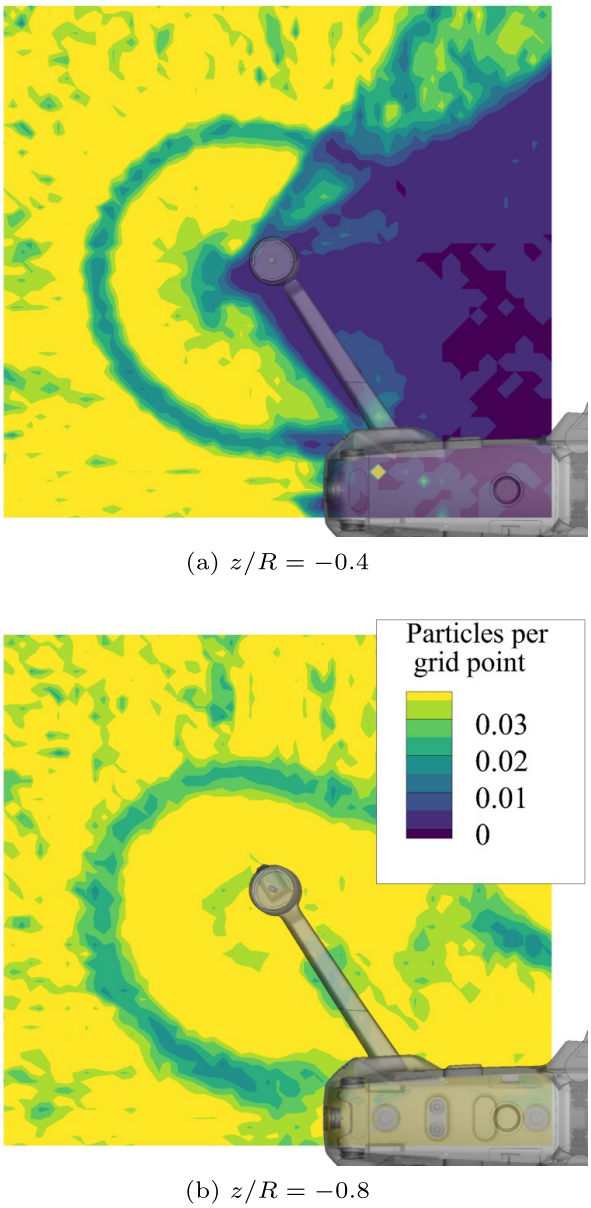

(a) $z/R = -0.4$

(b) $z/R = -0.8$

Fig. 9 Seeding density below the left back rotor, shown in a top-down view with a semi-transparent 3D model of the fuselage for illustration purposes

3 Results and discussion

3.1 Average flow field

A first overview of the quadcopter's volumetric wake evolution is given in Fig. 10 by means of the time-averaged and normalized vertical velocity, w/V_h, in slice planes at several z-coordinates below the quadcopter. The statistics account for approximately 2100 flow samples taken over 2.8 s.

At $z/R = -0.8$, Fig. 10a, the four rotor wakes appear as separate annular shapes. The velocity is small in the rotor centers, below the motor nacelles and at small rotational velocities of the blades, but increases toward the blade tip area. A closer look also reveals the wakes of the nacelle struts, and a higher velocity level below the front rotors due to the larger rotor frequency. (A quantitative analysis will be given in the next section.) In a distance of 2.5 rotor radii to the quadcopter, Fig. 10b, the individual annular structures wash out, before merging into a single and roughly circular wake structure as seen at 4.5 rotor radii below the quadcopter, Fig. 10c. However, even in a distance of 7.0 rotor radii, Fig. 10d, the wake is still not entirely rotationally symmetric. By tendency, the initial "X-shape" given by the layout of the

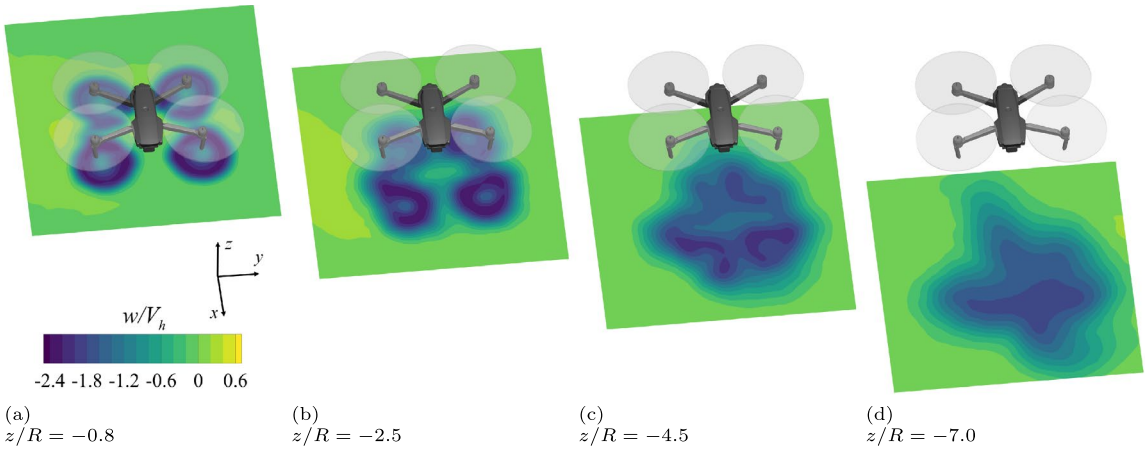

Fig. 10 Wake evolution in OGE hover, oblique top view, time-averaged downwash velocity w/V_h, $m = 915$ g

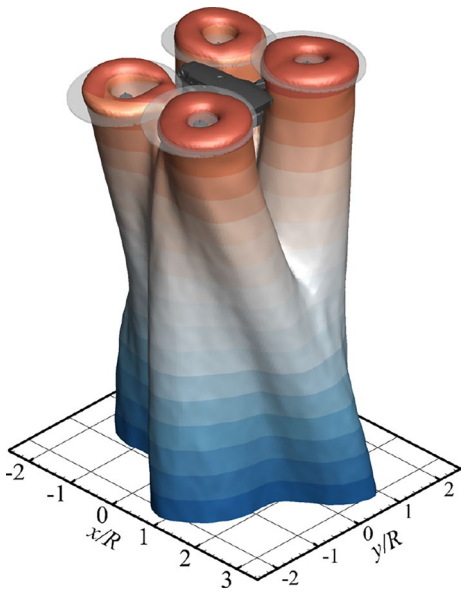

Fig. 11 Isosurface $w/V_h = -1$ in the time-averaged field, OGE hover with $m = 915$ g. The red-to-blue coloring corresponds to a decreasing z-position from $z/R = 1$ to $z/R = -7.5$

four rotors has developed into a "Plus-shaped" structure with velocity lobes aligned with the x- and y-axes.

A deeper insight into this development is given in Fig. 11 by means of the volumetric isosurface for $w/V_h = -1$, that is, the isosurface of the nominal hover-induced velocity. The left and right front wakes merge at about $z/R = -3.5$ into a single jet forming the high-velocity lobe approximately pointing along the positive x-axis (forward), and the same development is observed for the back rotors and a corresponding lobe along the negative x-axis (backward, not shown). Two additional lobes develop shortly below the rotor planes in lateral direction, pointing along the positive and negative y-axis. These lobes are consistent with the rotational directions shown in Fig. 2, with the spin of the opposing front and back rotors ejecting fluid in outboard direction. The four lobes create the "Plus-shaped" layout of the far wake, but its center is not perfectly aligned with the coordinate origin at $x = y = 0$. This is probably due to very large-scale flow structures occurring within the entire test enclosure, or due to the positional drift of the quadcopter during the test interval.

Figure 12a–c provides additional details of the wake flow in slices at $x/R = 0.98$, through the centers of the front rotor planes. The instantaneous sample (Fig. 12a) is affected by a multitude of small-scale turbulent structures, particularly developing in the shear layers between the rotor wakes and the external flow. Nevertheless, the overall flow structure is very similar to the corresponding time-average (Fig. 12b). The skewed left and right wakes are approximately perpendicular to the inward-tilted rotor planes (highlighted by red lines in Fig. 12b), indicating that the rotor tilt promotes the wake merging. In the central region of the wake, the downwash velocity exceeds a level of $w/V_h = -2.2$ in thin lobes stretching up to $z/R = -2$ below the quadcopter. The hover-induced velocity, V_h after Eq. (1), is calculated as an average for the front and rear rotors. Hence, the V_h-normalized velocity level in the front rotor wake is comparably high, since front rotor speed is 17% larger than the back rotor speed, see Table 1.

Adding a ballast of 220 g increases both V_h (from 4.9 to 5.5 m/s) and the absolute velocity levels in the wake. The resulting normalized velocity distributions w/V_h are almost identical to the result with the standard gross mass of $m = 915$ g, compare Fig. 12b and c. This indicates the validity of the normalization, and that the variation of m is not large enough to induce notable changes in the wake's structure.

The slice in Fig. 12d is at $x = 0$, in the center between front and back rotors. The velocity levels are smaller, but

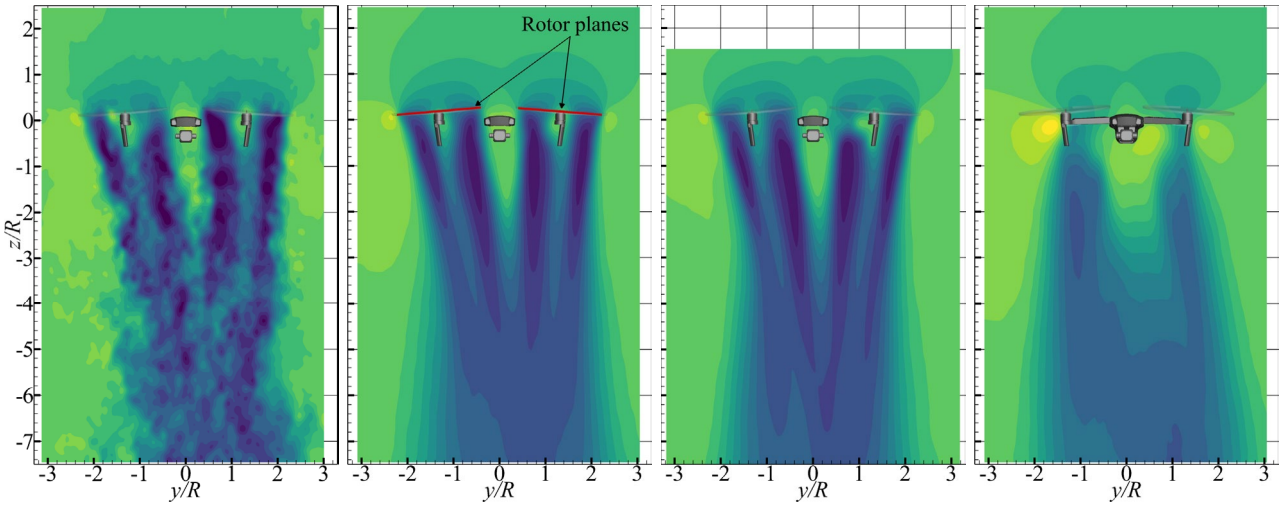

(a) Instantaneous sample, $x/R = 0.98$ (front rotors), $m = 915\,\mathrm{g}$

(b) Time-average, $x/R = 0.98$ (front rotors), $m = 915\,\mathrm{g}$

(c) Time-average, $x/R = 0.98$ (front rotors), $m = 1135\,\mathrm{g}$

(d) Time-average, $x = 0$ (center btw. front/back rotors), $m = 915\,\mathrm{g}$

Fig. 12 Time-averaged downwash velocity w/V_h in different x-slices, see Fig. 10 for the color legend

the wake's width is broader, since this slice coincides with the lateral velocity lobes developing in the center between front and back rotor. Yellowish areas left and right of the quadcopter indicate a positive w-component, i.e., a leakage of fluid in bottom-to-top direction. Unfortunately, this region falls into the particle shadow region of the rotors, preventing a detailed quantitative analysis.

3.2 Mass and momentum analysis

Calculating the instantaneous mass and momentum fluxes over suitable control volumes (CV) is often used in numerical or analytical studies, for example, to evaluate the integral loads on a body. Applying this concept to experiments is common for quasi-2D studies, for example when measuring the drag of an airfoil with a wake rake in a wind tunnel, but very rare in complex 3D flows due to a lack of suitable volumetric data. The current analysis of the volumetric flow fields uses a cubic CV aligned with the x, y, z-coordinate system, see Fig. 13, with the drone-fixed coordinate origin in its center. The CV consists of a top plane, four side planes, and a bottom plane. Each grid point on one of the six planes represents a plane increment with area dA (square of the grid spacing, here $dA = 25\,\mathrm{mm}^2$) and face normal unit vector $\vec{n}$.

Summing up the mass flux and the z-momentum flux (vertical direction) of all increments dA yields the incompressible continuity equation and the momentum equation as follows:

$$0 = -\sum_{\mathrm{CV}} \vec{n}\left(\vec{u}\rho\right) \mathrm{d}A \tag{3}$$

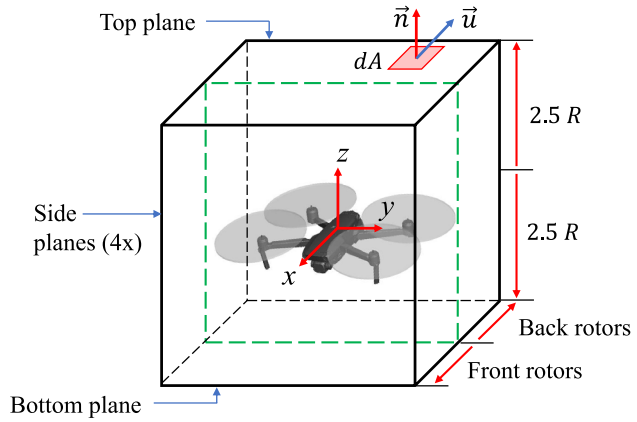

Fig. 13 Sketch of the control volume for mass and momentum analysis

$$F_z = -\sum_{\mathrm{CV}} \vec{n}\left(\vec{u}\rho\right) w \,\mathrm{d}A \tag{4}$$

Since the conservation of mass is enforced by a constraint during the FlowFit data assimilation, it is expected that Eq. (3) is fulfilled for any arbitrarily chosen CV in the flow field, within the numerical error bounds. Equation 4 yields the net vertical force F_z but neglects pressure terms, assuming a constant ambient pressure on all control planes. In the current case, this simplification is valid for the time-averaged field and if the distances of the CV top and bottom planes to the rotors and to the ground surface are large enough. For future implementations of FlowFit, a pressure reconstruction via the Poisson equation as an additional constraint is planned, see Godbersen et al. (2024), which facilitates

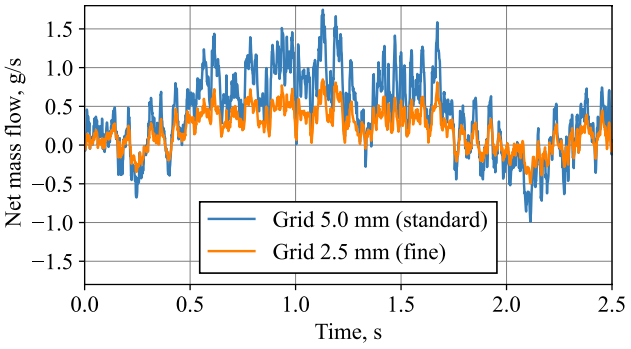

Fig. 14 CV net mass flow, OGE hover case

Table 2 Average mass flow breakdown, OGE hover case

Top plane (measured)	Side planes (measured)	Bottom plane (measured)	Rotor planes (estimate)
369 g/s	955 g/s	−1324 g/s	900 g/s

Table 3 Average momentum breakdown, OGE hover case

Rotors	Front (meas.)	Back (meas.)	All (meas.)	All (estimate)
T	5.32 N	3.90 N	9.21 N	8.98 N
C_T	0.01398	0.01378	0.01397	0.01361

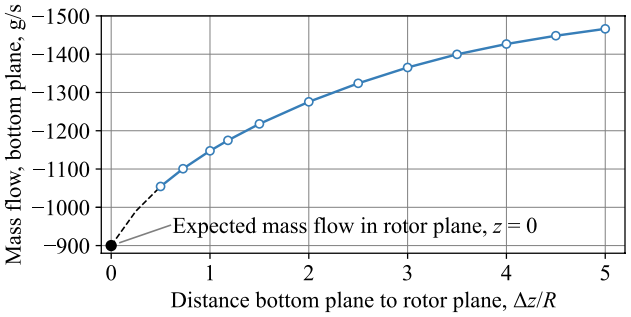

Fig. 15 Mass flow through the CVs bottom plane as a function of the vertical plane position below the quadcopter

an evaluation of the momentum equation including pressure terms. The following analysis considers an OGE hover case with standard gross mass ($m = 915$ g) and a CV size of $5\,R \times 5\,R \times 5\,R$ as sketched in Fig. 13.

Figure 14 shows the CV's instantaneous net mass flow (blue solid line) given by the right side of Eq. (3). For the standard grid resolution of 5 mm, the net mass flow is close to the expected value of zero, with a standard deviation of 0.50 g/s (gram per second) and an average of 0.40 g/s, indicating an apparent mass gain. However, these numbers are negligibly small in comparison with the overall mass flow through the control planes (details will be given later).

Applying a finer sampling grid resolution with a spacing of 2.5 mm but using the same particle track data and the same continuous flow field representation provided by FlowFit yields the second result (orange solid line) in Fig. 14. Both the standard deviation of 0.25 g/s and the average of 0.20 g/s for the net mass flow is halved in comparison with the coarser grid spacing of 5 mm. This indicates that the residual non-zero net mass flow is predominantly connected to discretization errors of the control volume.

The time-averaged contributions of individual planes to the net mass flow are given in Table 2, with top and side planes as net inflow (positive sign) and the bottom plane as net outflow (negative sign). There is no reliable experimental data for the mass flow through quadcopter's rotor planes, but an estimate derived from the hover-induced velocity is given by $V_h A_r \rho = 900$ g/s. The inflow through the top plane, 369 g/s, only covers 41% of this value, indicating a large contribution through the four side planes and above the rotors. On the other hand, the outflow though the bottom plane, 1324 g/s, is 47% larger than the nominal rotor plane flow. This indicates that the developing wake below the rotors has a strong entrainment effect on the external flow, which is also fed by the side planes and below the rotor.

Evaluating Eq. (4) yields a time-averaged vertical net force (thrust) of $F_z = T = 9.21$ N ($C_T = 0.01397$), which differs by only 2.6% from the expected value induced by the quadcopter's weight, $T \approx m\,g = 8.98$ N ($C_T = 0.01361$). Moreover, the CV can be split at $x = 0$ into a front half and a back half, see the green dashed line in Fig. 13. This yields thrust contributions of 5.32 N for the front subvolume and 3.90 N for the back subvolume, underlining the front-heavy load distribution of the quadcopter with a front-to-back ratio of 1.366. This result is very close to the expected value given by the squared ratio of the front and back rotor frequencies (Table 1) of $(94\ \text{Hz}/81\ \text{Hz})^2 = 1.347$, indicating very similar thrust coefficients for front and back rotors. The main results of the momentum equation are summarized in Table 3.

The conclusions drawn from the mass and momentum analyses are insensitive toward small changes of the CV's dimensions, but the strong entrainment effect of the wake motivates a variation of the distance between the CV's bottom plane and the quadcopter. Figure 15 shows the mass outflow (blue unfilled circles) through the bottom plane as a function of this distance, $\Delta z/R$. It is noted that the position of the top plane was kept constant, and that the side planes were shrunk/stretched according to the position of the bottom plane. The mass flow indeed increases with increasing $\Delta z/R$ due to entrainment effects, but at a declining rate. There is no reliable experimental data close to the rotor planes, but the continuation of the measured trend (black

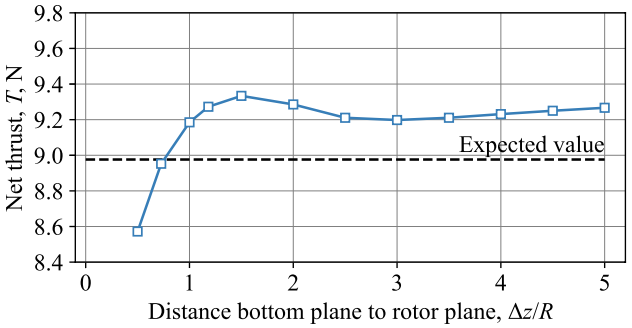

Fig. 16 CV thrust as a function of the CV bottom plane's vertical position below the quadcopter

dashed line) is consistent with an estimated rotor plane mass flow of -900 g/s at $z = 0$ (•). For example at $\Delta z/R = 5$, five rotor radii below the rotor planes, this mass flow has increased by 63% to -1466 g/s.

The corresponding results for the CV's net thrust are shown in Fig. 16 (blue unfilled squares). For distances with $\Delta z/R > 1$, the measured thrust shows some variations and is systematically larger than the expected value (black dashed line). The relative difference has a maximum of about 4%, occurring at a small thrust overshoot at $\Delta z/R = 1.5$. For $\Delta z/R < 1$, the calculated thrust strongly decreases with decreasing $\Delta z/R$. This is a consequence of the missing pressure data of the flow field. Toward the rotor planes, the velocity decreases, but the static pressure increases. Not factoring the latter term into the momentum equation yields an underestimation of the net thrust.

The CV's mass and momentum conclusions are supported by the distribution of the standard deviation of the streamwise velocity component, Std(w), as shown in Fig. 17. High levels of unsteadiness (partly exceeding 50% V_h) occur in the slipstream boundary between the rotor wake and the external flow, indicating a momentum exchange between low and high-velocity areas. This is observed well below the rotor planes, underlining the ongoing entrainment even up to $z/R = -7$. It is also noted that the shown Std(w)-distribution is fairly asymmetric with respect to $y = 0$ and below $z/R = -4$, which was not observed in the corresponding distribution of the average value, Fig. 12a. The reason for this asymmetry is not known, but probably related to large-scale flow structures in the test enclosure.

Overall, the analysis quantifies how the core wake interacts with the external flow via turbulent exchange, increasing the total mass flow while decreasing the mean velocity at a constant net momentum.

3.3 Ground effect

Figure 18a shows the time-averaged downwash velocity component w/V_h at $x/R = 0.98$ (center of the front rotors)

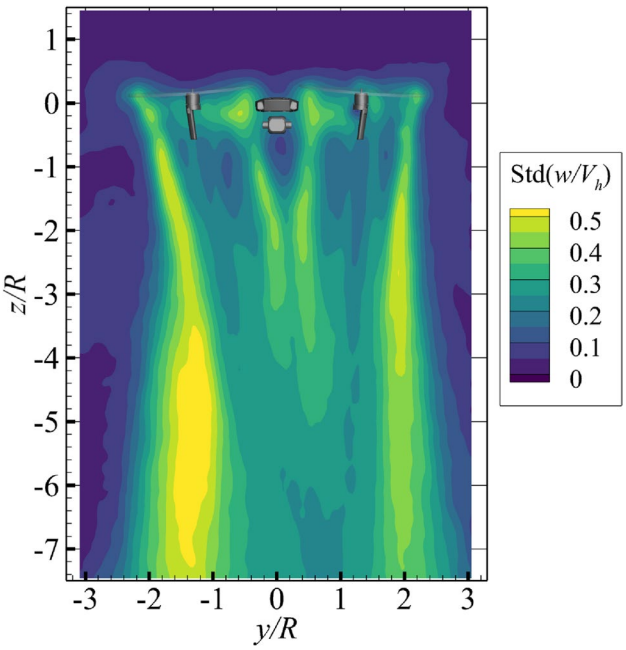

Fig. 17 Flow's unsteadiness, standard deviation of the downwash component w/V_h at $x/R = 0.98$, $m = 915$ g

for a hover test case with a normalized height of $h/R = 3.2$ above ground. The ground surface is visualized by the red line at the bottom. At this h/R, the ground has still no influence on the rotor efficiency, see Fig. 3, with $C_T = 0.0134$ and rotor speeds according to OGE conditions. Comparing the current flow field to the respective OGE result, see Fig. 10a, there is only a small reduction of the maximum downwash velocity ($w/V_h = -2.2$ versus $w/V_h = -2.3$). Other than that, the presence of the ground surface strongly alters the flow pattern. The narrowest point of the wake is at about $z/R = -1.5$. Below this point, the individual wakes of the left and right rotors no longer merge into a singular wake, but are split and deflected in outboard direction by the presence of the ground surface.

An even stronger difference is seen in the plane at $x = 0$ (between the front and back rotors), compare the current Fig. 18b to the OGE result in Fig. 12d. The ground surface results in a strong upwash region below the fuselage, see the yellow coloring marked by a red arrow, indicating a recirculation (fountaining) area. The maximum upwash is $w/V_h = 0.9$ at $z/R = -1.0$ below the quadcopter.

The average volumetric flowfield is used to visualize the structure of this recirculation by means of 3D streamlines, see Fig. 19a for an oblique left side view. Streamline I crosses the left rear rotor plane in its frontal half. The fluid is accelerated in downward direction, before it is deflected in outward direction by the ground surface, as expected for the "normal" IGE flow field. Streamline II crosses the same rotor plane in a further inboard position. Below the

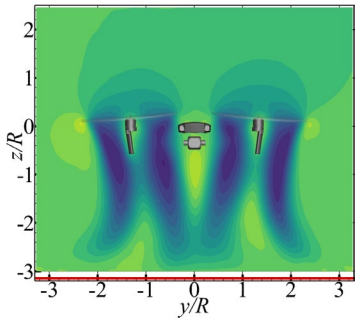

(a)
$h/R = 3.2, x/R = 0.98$ (front rotors)

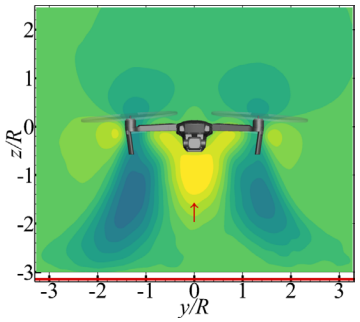

(b)
$h/R = 3.2, x = 0$ (btw. front/back rotors)

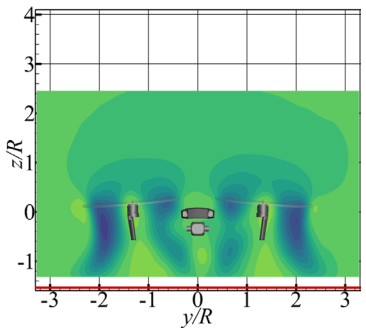

(c)
$h/R = 1.6, x/R = 0.98$ (front rotors)

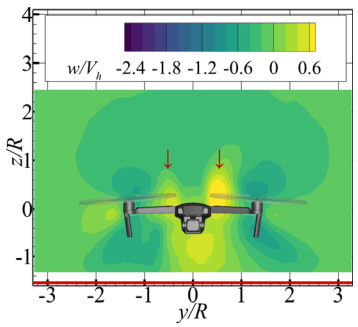

(d)
$h/R = 1.6, x = 0$ (btw. front/back rotors)

Fig. 18 Average downwash velocity w/V_h for different IGE hover heights h/R, $m = 915$ g

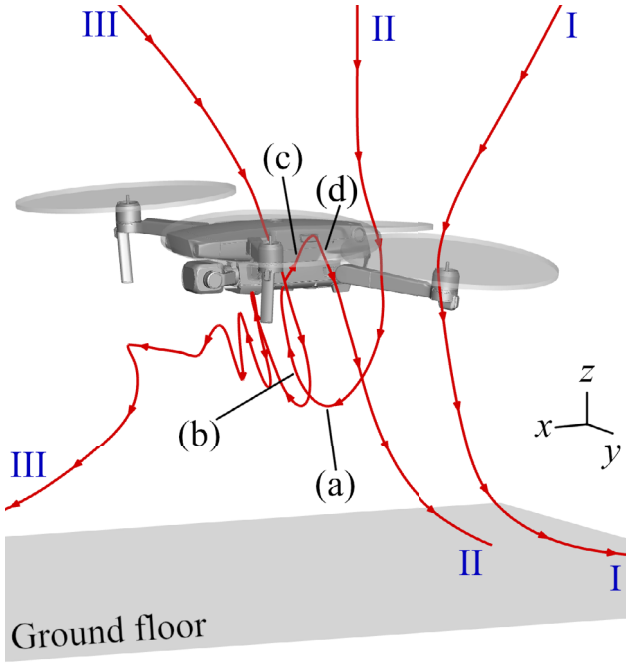

(a) Oblique left side view

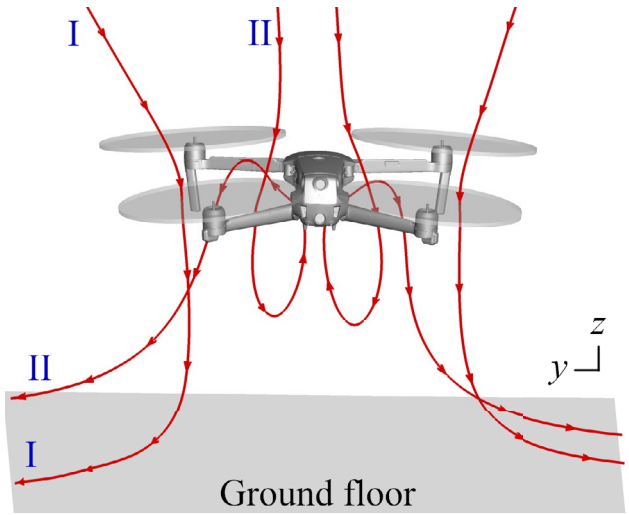

(b) Rear view

Fig. 19 Streamlines in the time-averaged flow field, IGE hover with $h/R = 3.2$ and $m = 915$ g, also see Fig. 18a, b

rotor at about $z/R = -1.5$, the streamline bends in inboard and forward direction (a), where it enters the recirculation zone moving against the main flow direction and toward the fuselage (b). The fuselage then deflects the streamline in outboard direction (c) and into the zone of influence of the front rotor (d). From this point on, the streamline follows a "normal" behavior along the IGE wake without further recirculation. For a better understanding of the flow's spatial organization, streamlines I and II are repeated in a rear view shown in Fig. 19b. Additionally, the figure shows two corresponding streamlines on the right side of the drone, indicating that the overall flow is approximately symmetric toward $y = 0$.

Streamline III in Fig. 19a crosses the plane of the left front rotor in an inboard position. Similar to streamline II, it is also entrained into the recirculation area. Here, the streamline passes three entire loops while simultaneously convecting in forward direction, before being ejected into the front rotor's wake. It is noted that due to unsteadiness, the actual trajectories of the HFSB tracer bubbles will differ from the average flow, and that the reconstructed flow close to the rotor planes is less reliable due to the lack of particle data. Nevertheless, the streamlines of the time-averaged flow are still expected to give a good overview of the recirculation's volumetric structure.

Figure 18c and d corresponds to a reduced hover height of $h/R = 1.6$. Due to a constant gross mass of $m = 915$ g but an increased IGE rotor efficiency, the average rotor frequency is lowered, and the thrust coefficient increases by about 7% (from $C_T = 0.0134$ to $C_T = 0.0143$, see Fig. 3 and Eq. 2). The maximum downwash velocity in the plane of the front rotors ($x/R = 0.98$, Fig. 18c) reduces from $w/V_h = 2.2$ to $w/V_h = 1.9$. The small ground clearance also partly inhibits the recirculation below the fuselage ($x = 0$, Fig. 18d), even though there is still a small yellowish area with a positive w-velocity component. In addition, two new yellow lobes with $w > 0$ develop left and right of the fuselage, see the red arrows in Fig. 18d. These lobes indicate a leakage of fluid in upward direction between the front and back rotors. The flow field supports the idea that the quadcopter hovers on a self-induced high-pressure air cushion when flying very close to the ground.

Moreover, it is noted that the presented test cases are compatible with Dekker et al. (2022)'s categories derived from a generic side-by-side rotor configuration in ground effect, namely "merged wake" (OGE case, as in Fig. 12b), "fountain flow" (IGE $h/R = 3.2$, as in Fig. 18a, b), and "fountain flow re-ingestion" (IGE $h/R = 1.6$, as in Fig. 18c, d).

Looking at the azimuthal variation of the quadcopter's outwash along the ground surface, the "Plus-shaped" pattern already observed in the OGE cases is now strongly amplified, see Fig. 20.

The shown z-planes were selected in a height of $0.25\,h/R$ above ground, or $z = -0.75\,h/R$ below the quadcopter. The coloring corresponds to the average radial velocity, v_r, calculated from the in-plane components u, v and with respect to the origin at $x = y = 0$. Thin spike-like areas with high outwash velocities, $v_r/V_h > 1.3$, develop in both longitudinal and lateral directions along the confluence lines of the individual wakes. The spikes in lateral direction are not perfectly aligned with the y-axis but slightly tilted in backward direction, which is probably a result of the larger mass flow of the faster-spinning front rotors. It is noted that the interaction of multiple rotors in ground effect and the resulting azimuth-dependent outwash characteristics have been investigated extensively in the context of operational safety of helicopters

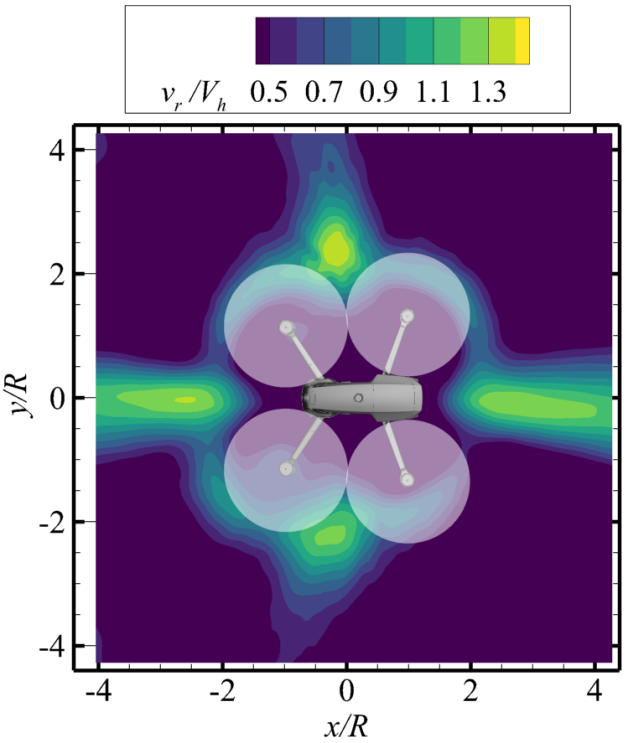

(a) Hover height $h/R = 3.2$

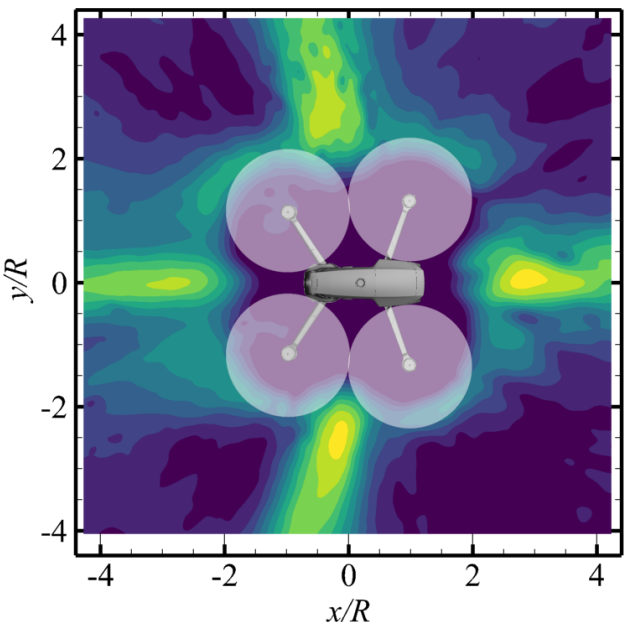

(b) Hover height $h/R = 1.6$

Fig. 20 Average outwash footprint, radial velocity v_r in a plane $0.25\,h/R$ above ground, $m = 915$ g

with tandem main rotors, e.g., see Silva and Riser (2011). The current focus on eVTOL vehicles with distributed propulsion motivates the investigation of multi-rotor configurations, see Brown (2023) or Bain et al. (2024).

3.4 Forward flight case

This section considers the quadcopter in horizontal forward flight with a velocity of 3.1m/s (about 0.63 V_h), outside of ground effect and with the standard gross mass of $m = 915$ g. The flight direction is aligned with the left–right direction of the test enclosure, almost utilizing its entire breadth of 6 m. Nevertheless, the attainable flight speeds are significantly smaller than the quadcopter's maximum free-flight velocity of 20 m/s.

Figure 21 visualizes the extension and structure of the wake by means of instantaneous vortical structures as seen by isosurfaces of the Q-criterion. As in the hover cases, the origin of the coordinate system was set to the center of the four rotors. The x-axis is in horizontal direction pointing along the flight path, independent of the quadcopter's nose-down pitch angle. The wake skew angle is obvious in the side view shown in Fig. 21a. The spatial resolution is not suitable to quantify individual small-scaled vortical events, but between four and five blade tip vortices (2-2.5 rotor revolutions) are visible directly below the rotor planes, before developing into smaller structures. The frontal view in Fig. 21b partly lacks the two youngest blade tip vortices on the quadcopter's left side (right side of the figure). In forward flight, the test enclosure's glass panels and the camera system are on the right side of the quadcopter, yielding larger shadow regions (void of particle tracks) and unreliable velocity data on its left side.

The most remarkable observation during the forward flight experiments and the subsequent post-processing of the particle tracks was the appearance of large-scale coherent, longitudinal vortices left and right of the rotor downwash. In this area, the particle motion has a striking resemblance to wingtip vortices observed when fixed-wing aircraft flying through clouds or fog. The occurrence of such counterrotating trailing "supervortices," fed by the blade tip vortices, is well-known for helicopters in forward flight, e.g., see Ahmad and Chaderjian (2011) and many others. Moreover, recent publications focusing on multi-rotor eVTOL vehicles have reported that this is an universal phenomenon independent of the rotor configuration, for example see Caprace and Ning (2023). The understanding of the initial roll-up procedure will strongly benefit from volumetric experimental data.

Despite having a notable circulation strength, the supervortices are hard to identify in the current instantaneous field and with gradient-based detection criteria (such as the Q-criterion in Fig. 21). Hence, the time-averaged flow field is calculated, eliminating small-scale turbulence and washing out the blade tip vortices, whose position depends on the rotor azimuth angle.

Time-averaging the velocity data in a quadcopter-fixed moving reference frame is difficult in forward flight cases, partly due to the manual piloting in the confined space of the test enclosure, including acceleration and deceleration maneuvers. Even when the quadcopter's flight path is positioned well with respect to the high-speed cameras, it quickly traverses the illuminated measurement volume within fractions of a second. For the test case in Fig. 21, the average flow field was calculated over 63 instantaneous volumetric flow fields, corresponding to 84 ms at a sampling rate of 750 Hz, or 3% of the samples factored into the hover

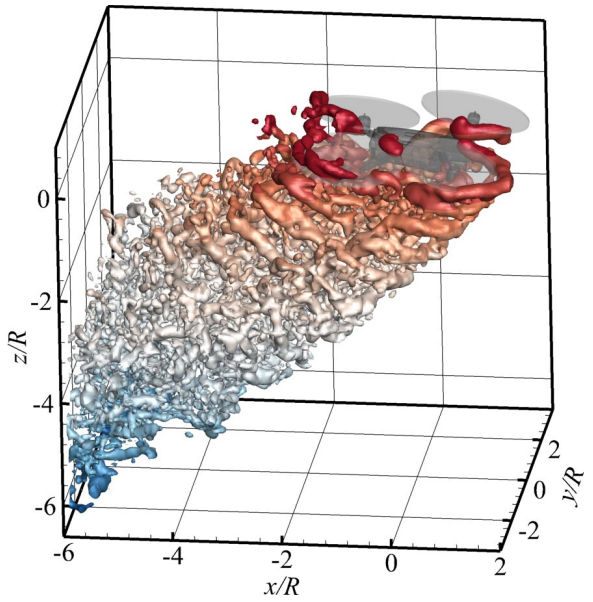

(a) Oblique right side view, the quadcopter moves left to right

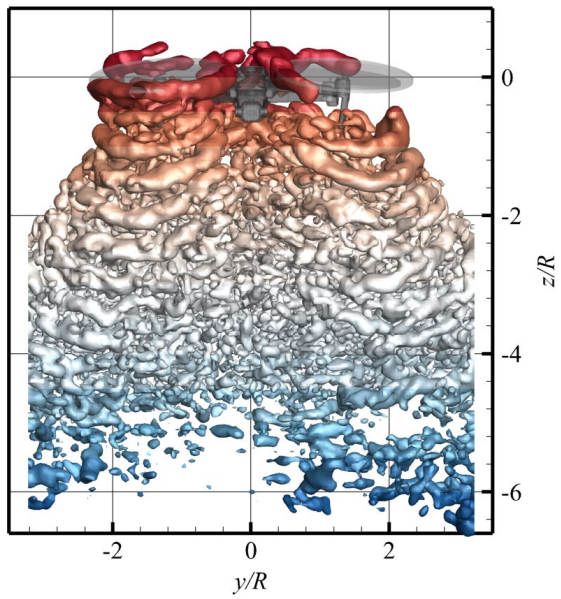

(b) Frontal view, the quadcopter moves towards the observer

Fig. 21 OGE forward flight, instantaneous Q-criterion, isosurface value $1.5 \times 10^4/s^2$. The red-to-blue coloring corresponds to a decreasing z-position from $z = 0$ to $z/R = -6$

statistics. Figure 22 shows the time-averaged downwash component w/V_h in different x-slices.

The wakes of the front rotors are seen in the upper parts of the slices corresponding to the front rotor centers ($x = 0.98$, Fig 22a) and between the front and back rotors ($x = 0$, Fig. 22b). The maximum downwash levels are approximately $w/V_h = -2.2$ and very similar to the corresponding hover results (Fig. 12b and c). In contrast to the hover cases, yellowish areas of positive (upward) flow appear along the left and right shoulders of the front rotor wakes. The vectors in Fig. 22 refer to the average in-plane components v, w but are only shown at every third grid point in both y, z-directions, and clearly prove the generation of a set of counterrotating large-scale vortices. In addition to the wake's downwash component, there is a notable velocity component in negative x-direction (not shown, up to $u/V_h = -1.2$) providing the propulsive thrust in forward flight.

The slice at the rear end of the back rotor planes, $x/R = -2$ in Fig 22c, illustrates that the skewed flow in forward flight leads to a close proximity of the front and back rotor wakes and, thereby, to an earlier merging. This trend continues downstream of the quadcopter, for example at $x/R = -3.5$ shown in Fig. 22d, where the wakes of individual rotors can no longer be differentiated. However, the pair of counterrotating vortices is still visible, with the rotational centers marked by red arrows in Fig. 22d.

A better understanding of the flowfield is given by the volumetric streamlines in Fig. 23. The lateral origin of the streamlines I to V was set to the outmost blade tip positions of the right rotors, and the horizontal origins were distributed between the front and back rotor axes.

Streamlines I and II originate from the front rotor's sphere of influence, both streamlines rotate around each other and form the core of the right supervortex. The origin of streamline III is between the front and back rotors, and this streamline is also entrained into a very wide circular motion in the peripheral area of the supervortex. The supervortex also strongly bends the streamlines IV and V (originating from the back rotor) in outward direction, but these streamlines are not entrained into a full circular motion. The front rotors ("bearhug" mode) create stronger blade tip vortices in the outboard positions, where the blade motion is against the forward flight motion, in comparison with the back rotors ("breaststroke" mode), which move with the inflow direction. Hence, it is plausible that the forming supervortices are predominantly fed by the front rotors.

The frontal view in Fig. 23b also shows streamlines on the left side of the quadcopter (despite the higher uncertainty due to the shadowed region close to the rotor plane, Fig. 22), using the same origins but with mirrored y-coordinates. Similar to preceding results, the flowfield is not entirely symmetric, but the general conclusions are the same as on the left side.

4 Conclusion

For the first time, the aerodynamics of a free-flying model-sized quadcopter with an overall span of 0.5 m was investigated using Shake-The-Box Lagrangian particle tracking, allowing to study the time-resolved three-dimensional flow field in a measurement volume with an overall size larger than 1.5 m^3.

The results provide a deeper insight into the complex aerodynamic interactions of the multi-rotor configuration and its fuselage. A focus was set on the development of the wake structure in the quadcopter's reference frame, and the following details:

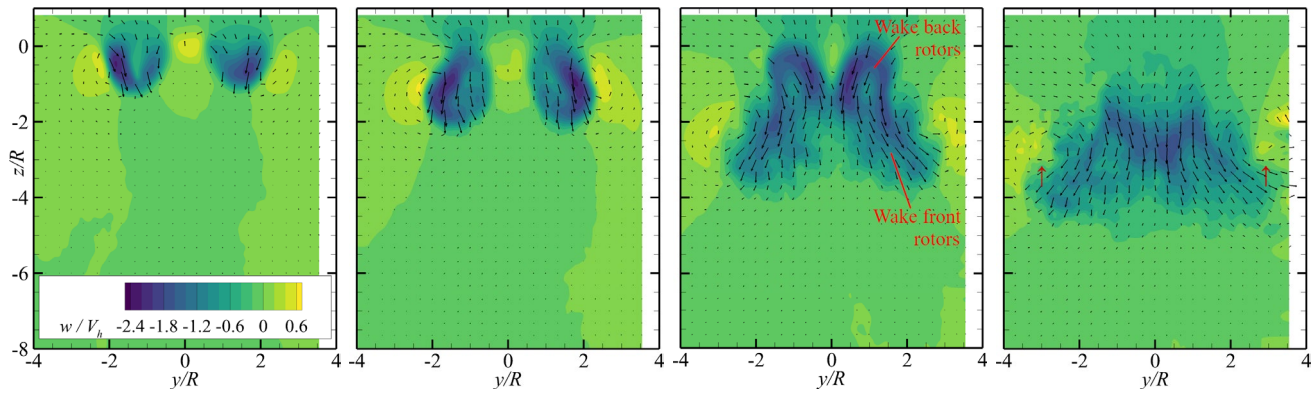

Fig. 22 Average downwash velocity w/V_h and in-plane v, w-velocity vectors in different x-planes.

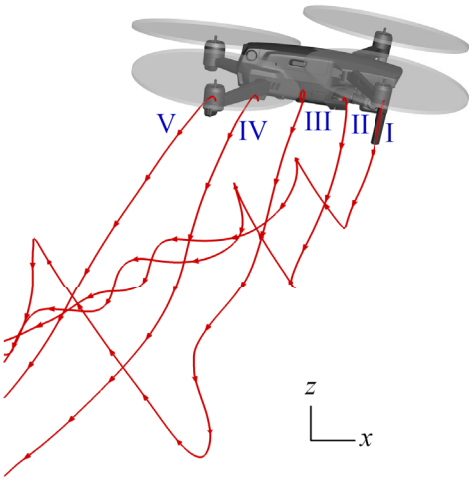

(a) Right side view, the quadcopter moves left to right

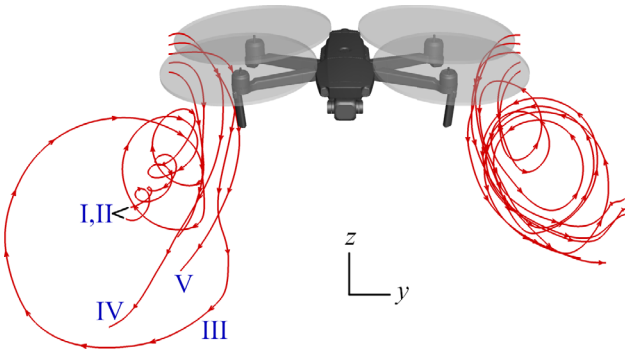

(b) Frontal view, the quadcopter moves towards the observer

Fig. 23 OGE forward flight, streamlines in the average volumetric flow field

1. For hover out of ground effect, the four rotor wakes are skewed according to the inward tilt of the individual rotor planes, and successively merge into a single wake between about three and five rotor radii below the quadcopter. The resulting wake is not rotationally symmetric, but develops lobes along the dividing lines between the rotors.
2. Defining appropriate control volumes and applying the conservation of mass and momentum provides accurate estimates for the quadcopter's total thrust, and for the thrust distribution between individual rotors. Furthermore, a rapid increase in the wake's mass flow through entrainment of external flow at a constant overall momentum was quantified. For example, the mass flow at three rotor radii below the quadcopter is about 50% larger than the nominal mass flow through the rotor planes.
3. When hovering in moderate ground effect (here: $h/R = 3.2$), the ground surface inhibits the wake merging and deflects the individual rotor wakes in radially outward direction. This also results in the formation of a large-scale recirculation zone below the fuselage, fed by the inner areas of both front and back rotors. For very low hover heights (here: $h/R = 1.6$), both the recirculation zone and the downwash velocities are reduced, as the quadcopter hovers on a self-induced air cushion. In both hover heights, the radial outwash flow along the ground surface shows a strong azimuthal dependency, with high-velocity spikes in a "Plus-shaped" pattern along the lateral and longitudinal axes of the quadcopter.
4. Moderate forward flight conditions (3.1 m/s, or 63% of the hover-induced velocity V_h) yields a notable wake skew angle. Consequently, the reduced separation between front and back rotor wakes promotes a rapid merging of the individual rotor wakes. Forward flight also results in the formation of longitudinally aligned trailing "supervortices," similar to the wingtip vortices of a fixed-wing aircraft. Tracing the streamlines in the time-averaged volumetric flow field implies that these vortices are primarily fed by the outer parts of the front rotor's blade tip vortices.

In a next step, the results will be prepared as a reference data set for comparisons to mid- and high-fidelity numerical simulations, including a digitization of the fuselage and rotor geometries.

Acknowledgements This study was conducted within the framework of the DLR projects "URBAN–Rescue" and "ROME." The authors would like to thank Janos Agocs, Tobias Kleindienst, Kevin Kienass, Carsten Fuchs, Tobias Herrmann, Johannes Braukmann, and Markus Krebs for their support during the setup of the test campaign.

Funding Open Access funding enabled and organized by Projekt DEAL.

References

Ahmad JU, Chaderjian NM (2011) High-order accurate CFD/CSD simulation of th UH-60 rotor in forward flight. In: 29th AIAA Applied Aerodynamics Conference, Paper AIAA 2011-3185, Honolulu, HI, 27–30 June 2011, https://doi.org/10.2514/6.2011-3185

Bain J, Nikolaev S, Chavez R et al (2024) Outwash measurement of Joby pre-production prototype. In: American Helicopter Society

80th Annual Forum, Montréal, Canada, 7–9 May 2024, https://doi.org/10.4050/F-0080-2024-1380
Bodling A, Potsdam M (2022) Numerical investigation of secondary vortex structures in a rotor wake. J Am Helicopter Soc 67(4):1–18. https://doi.org/10.4050/JAHS.67.042007
Bodling A, Schwarz C, Wolf CC et al (2024) Enhancing numerical accuracy in the prediction of rotor wake structures. Phys Fluids 36(037137):1–16. https://doi.org/10.1063/5.0196010
Brown RE (2023) Understanding the downwash/outwash characteristics of eVTOL aircraft. Report CAP 2576A prepared for the UK Civil Aviation Authority
Caprace DG, Ning A (2023) Large eddy simulation for empirical modeling of the wake of three urban air mobility vehicles. J Am Helicopter Soc 68(042002):1–16. https://doi.org/10.4050/JAHS.68.042002
De Gregorio F, Rossignol KS, Ceglia G, et al. (2023) Multi-rotor wake interaction characterization. In: 49th European Rotorcraft Forum, Bückeburg, Germany, 5–7 September 2023
Dekker HNJ, Ragni D, Baars WJ et al (2022) Aerodynamic interactions of side-by-side rotors in ground proximity. AIAA J 60(7):4267–4277. https://doi.org/10.2514/1.J061105
DJI (2024) Mavic 2. Manufacturer's homepage with technical specifications. https://www.dji.com/mavic-2/info (accessed 18 July 2024)
Gesemann S, Huhn F, Schanz D et al (2016) From noisy particle tracks to velocity, acceleration and pressure fields using B-splines and penalties. In: 18th International Symposium on Applications of Laser and Imaging Techniques to Fluid Mechanics, Lisbon, Portugal, 4–7 July 2016
Godbersen P, Gesemann S, Schanz D et al (2024) FlowFit3: Efficient data assimilation of LPT measurements. In: 21st International Symposium on Applications of Laser and Imaging Techniques to Fluid Mechanics, Lisbon, Portugal, 8–11 July 2024, https://doi.org/10.55037/lxlaser.21st.216
Kostek AA, Braukmann JN, Lößle F et al (2024) Experimental investigation of quadrotor aerodynamics with computational cross-validation. J Am Helicopter Soc 69(022009):1–17. https://doi.org/10.4050/JAHS.69.022009
Lim JW, Thai AD (2023) Variable rotor speed trim and interactional aerodynamics for quadcopter UAS. In: 49th European Rotorcraft Forum, Bückeburg, Germany, 5–7 September 2023
Nargi RE, De Gregorio F, Candeloro P et al (2021) Evolution of flow structures in twin-rotors wakes in drones by time-resolved PIV. J Phys: Conf Ser 1977(012008):1–20. https://doi.org/10.1088/1742-6596/1977/1/012008
Otsuka H, Kohno M, Nagatani K (2017) Flow visualization of wake of a quad-copter in ground effect. In: 6th Asian/Australian Rotorcraft Forum, Kanazawa, Japan, 7–9 November 2017
Sanchez-Cuevas P, Heredia G, Ollero A (2017) Characterization of the aerodynamic ground effect and its influence in multirotor control. Int J Aerosp Eng 1823056:1–17. https://doi.org/10.1155/2017/1823056
Schanz D, Gesemann S, Schröder A et al (2013) Non-uniform optical transfer functions in particle imaging: Calibration and application to tomographic reconstruction. Meas Sci Technol 24(024009):1–15. https://doi.org/10.1088/0957-0233/24/2/024009
Schanz D, Gesemann S, Schröder A (2016) Shake-The-Box: Lagrangian particle tracking at high particle image densities. Exp Fluids 57(70):1–27. https://doi.org/10.1007/s00348-016-2157-1
Schanz D, Novara M, Schröder A (2021) Shake-The-Box particle tracking with variable time-steps in flows with high velocity range (VT-STB). In: 14th International Symposium on Particle Image Velocimetry, Chicago, IL, 1–4 August 2021
Schanz D, Schröder A, Bosbach J et al (2024) Scanning Lagrangian particle tracking to measure 3D large scale aerodynamics of quadcopter flight. In: 21st International Symposium on Applications of Laser and Imaging Techniques to Fluid Mechanics, Lisbon, Portugal, 8–11 July 2024, https://doi.org/10.55037/lxlaser.21st.215
Schröder A, Schanz D (2023) 3D Lagrangian particle tracking in fluid mechanics. Ann Rev Fluid Mech 55:511–540. https://doi.org/10.1146/annurev-fluid-031822-041721
Schröder D, Leweke T, Stumpf E (2023) High-speed volumetric particle tracking measurements of unstable helical vortex pairs. Exp Fluids 64(141):1–14. https://doi.org/10.1007/s00348-023-03679-8
Shirazi D (2022) Comparison of the CHARM predictions of the multirotor test bed with wind tunnel experimental results. In: Vertical Flight Society Aeromechanics for Advanced Vertical Flight Technical Meeting, San Jose, CA, 25–27 January 2022
Shukla D, Komerath N (2018) Multirotor drone aerodynamic interaction investigation. Drones 2(4):1–13. https://doi.org/10.3390/drones2040043
Silva MJ, Riser R (2011) CH-47D tandem rotor outwash survey. In: American Helicopter Society 67th Annual Forum, Virginia Beach, VA, 3–5 May 2011
Tanabe Y, Sugawara H, Sunada S et al (2021) Quadcopter drone hovering in ground effect. J Robot Mechatron 33(2):339–347. https://doi.org/10.20965/jrm.2021.p0339
Throneberry G, Takeshita A, Hocut CM et al (2022) Wake propagation and characteristics of a multi-rotor unmanned vehicle in forward flight. Drones 6(5):1–19. https://doi.org/10.3390/drones6050130
Ventura Diaz P, Yoon S (2018) High-fidelity computational aerodynamics of multi-rotor unmanned aerial vehicles. In: AIAA SciTech Forum, Kissimmee, FL, 8–12 January 2018, https://doi.org/10.2514/6.2018-1266
Viola IM, Nila A, Davey T et al (2022) Underwater LED-based Lagrangian particle tracking velocimetry. J Vis 25(5):1035–1046. https://doi.org/10.1007/s12650-022-00832-z
Whidborne JF, Mendez A, Cooke A (2022) Effect of rotor tilt on the gust rejection properties of multirotor aircraft. Drones 6(10):1–24. https://doi.org/10.3390/drones6100305
Wieneke B (2008) Volume self-calibration for 3D particle image velocimetry. Exp Fluids 45:549–556. https://doi.org/10.1007/s00348-008-0521-5
Wolf CC, Schwarz C, Kaufmann K et al (2019) Experimental study of secondary vortex structures in a rotor wake. Exp Fluids 60(175):1–16. https://doi.org/10.1007/s00348-019-2807-1
Yonezawa K, Akiba K, Liu H et al (2021) Numerical investigations of ground effect of a quadcopter. In: The Proceedings of the 2021 Aisa-Pacific International Symposium on Aerospace Technology (APISAT 2021), Jeju, Korea, 15–17 November 2021, https://doi.org/10.1007/978-981-19-2689-1_57
Yoon S, Ventura Diaz P, Boyd Jr. DD et al (2017) Computational aerodynamic modeling of small quadcopter vehicles. In: American Helicopter Society 73th Annual Forum, Fort Worth, TX, 9–11 May 2017